

# Flow Control on Propeller Tip Vortex Cavitation through Water Jets

Liushuai Cao<sup>1</sup>, Kang Liu<sup>2</sup>, Decheng Wan<sup>1\*</sup>

<sup>1</sup> Computational Marine Hydrodynamics Lab (CMHL), School of Naval Architecture, Ocean and Civil Engineering,  
Shanghai Jiao Tong University, Shanghai, China

<sup>2</sup> China Ship Scientific Research Center (CSSRC), Wuxi, China

\* Corresponding author: dcwan@sjtu.edu.cn

## ABSTRACT

Tip vortex cavitation (TVC) of a propeller can significantly increase flow noise and vibration, resulting in reduced efficiency. Therefore, predicting the development of TVC and exploring control methods is of great value. We investigated the potential for controlling propeller TVC through active water jets. Utilizing large eddy simulation and the Schnerr-Sauer cavitation model, we studied the TVC of the INSEAN E779A propeller. Open water characteristics and cavitation results were analyzed and compared with experimental data. Subsequently, seven holes were opened on the center line (top injection), pressure side (pressure side injection), and suction side (suction side injection) of the propeller blade tip. Active water jets were released from these holes to control the TVC. Results indicated that the vortices on the propeller's surface developed outward along the radial direction due to the centrifugal force during rotation. Top injection had a limited effect on reducing the development length of TVC. However, injecting water on both the pressure side and suction side effectively inhibited TVC development, albeit causing structural deformation of the propeller sheet cavitation in both cases.

## Keywords

Flow control, propeller, tip vortex cavitation, water jets, Schnerr-Sauer model

## 1 INTRODUCTION

Cavitation is a periodic process in which vapor bubbles are formed, evolve, and gradually collapse and disappear during the phase transition of fluid between vapor and liquid (Franc & Michel 2006). Cavitation is a double-edged sword. It can be utilized for cleaning purposes in daily life. However, in most cases, cavitation remains a potentially harmful physical phenomenon. It can reduce the efficiency of machinery, generate noise, and cause material erosion.

The fundamental parameter in describing the physics of the process is the cavitation number, defined by

$$\sigma = \frac{P_{\infty} - P_v}{\frac{1}{2} \rho U_{\infty}^2} \quad (1)$$

wherein  $P_{\infty}$  and  $U_{\infty}$  are a characteristic pressure and velocity, respectively,  $\rho$  is the density, and  $p_v$  is a vapor

pressure. When cavitation has not occurred, the inception cavitation number can be used to describe the ease of cavitation in the flow field. After cavitation has occurred, the cavitation number can then be used to describe the development process of cavitation.

Cavitation can be classified into several types: bubble cavitation, sheet cavitation, cloud cavitation, super cavitation, and vortex cavitation. Among them, vortex cavitation can be further divided into tip vortex cavitation (TVC) and hub vortex cavitation based on the location of cavitation occurrence (Salvatore et al 2009). TVC is one of the common types of vortex cavitation, often occurring within the tip vortex. In the marine industry, cavitation is prone to occur in the tips of hydrofoils, rudders and propellers. Unlike sheet cavitation or cloud cavitation, TVC generally does not adhere extensively to the surface of the equipment. Therefore, it does not significantly affect the propulsion efficiency and lifespan of propellers. However, TVC can extend over a considerable distance as the fluid flows backward. During this process, the inception and collapse of cavities can lead to a significant increase in pressure pulsations, thus generating fluid noise. Moreover, due to the development of TVC, the equipment behind it is also highly susceptible. Therefore, investigating control methods for tip vortex and its cavitation is essential.

Currently, flow control is highly effective in controlling the generation and development of cavities. This method can be divided into two main categories: passive control and active control. Passive control often involves influencing the flow trends in the cavitation region by optimizing the shape of the equipment. For example, creating grooves in the leading-edge or adding vortex generators can alter the pressure distribution on the surface, thereby reducing the cavitation area. In recent years, this method has been widely used in the field of cavitation suppression (Kadivar et al 2018; Zhang et al 2022).

Unlike passive control methods, the primary idea behind active control is to introduce mass and momentum into the flow field to control the flow. This typically involves injecting water, air, or other polymers that inhibit cavitation near the cavitation region to improve the flow

conditions. To avoid pollution in the marine environment, water is the most commonly used jetting medium in active control methods. Implementing active control is more complex as pipelines for fluid injection need to be incorporated into the propeller. Additionally, extra jetting equipment needs to be introduced. The upfront investment and ongoing maintenance costs are higher for active control. However, this method allows for precise adjustments to the jetting equipment based on changes in operating conditions, enabling accurate regulation of cavitation suppression.

The control effect of jets on cavitation has been a popular topic of research. Scholars have applied active jetting methods to cavitation suppression based on experimental approaches. As early as 1993, Chahine et al (1993) attempted to use jetting of various compounds to suppress tip vortex cavitation on propellers and achieved good experimental results. Wang et al (2020) studied the effect of jets on the cavitation of the NACA66 (MOD) hydrofoil. Results showed that active jets could effectively reduce the occurrence of sheet cavitation and cloud cavitation on the hydrofoil. The location and velocity of the perforated jets also influenced their inhibitory effect. Timoshevskiy et al (2017) combined experimental and numerical methods to study the effect of tangential jets on the suction surface of a 2D hydrofoil. The results showed that tangential jets could effectively reduce the area of sheet cavitation, achieving effective suppression. Park et al (2014) combined active and passive jetting methods and verified the inhibitory effect of this approach on TVC. Lu et al (2018) implemented perforated jets on the suction surface of the NACA0066 hydrofoil, achieving efficient suppression of both sheet and cloud cavitation on the hydrofoil. In the same year, Lee et al (2018) conducted experiments applying jets separately to an elliptical hydrofoil and a propeller. They investigated the effect of jets on tip vortex cavitation and analyzed the resulting noise. The results showed that jets had a significant inhibitory effect on cavitation, with higher jet velocities leading to more pronounced cavitation delay. Additionally, jets effectively reduced the noise associated with cavitation.

This article intends to conduct a numerical simulation analysis of TVC and its control through water jets under different operating conditions. It begins by studying the open-water performance and cavitation of the INSEAN E779A propeller to validate the applicability of the numerical methods. Subsequently, the inhibitory effects of perforated jet flows on the propeller's tip vortex and TVC are explored. Finally, conclusions summarizing the content and findings of this paper are derived.

## 2 NUMERICAL METHODS

### 2.1 Large Eddy Simulation

Cavitation is an extremely complex turbulent flow involving the phase change between vapor and liquid. It is significantly influenced by the turbulent motion of the flow. Large eddy simulation (LES) is an inherently

transient technique in which the large scales of the turbulence are directly resolved everywhere in the flow domain, and the small-scale motions are modeled. For this approach, the computational grid determines the scales of the eddies that are filtered out. Inserting the decomposed solution variables into the Navier-Stokes equations results in equations for the filtered quantities (Bensow & Bark 2010). The filtered mass, momentum, and energy transport equations can be written as:

$$\frac{\partial \rho}{\partial t} + \nabla \cdot (\rho \tilde{\mathbf{v}}) = 0 \quad (2)$$

$$\begin{aligned} \frac{\partial}{\partial t} (\rho \tilde{\mathbf{v}}) + \nabla \cdot (\rho \tilde{\mathbf{v}} \otimes \tilde{\mathbf{v}}) \\ = -\nabla \cdot \tilde{p} \mathbf{I} + \nabla \cdot (\tilde{\mathbf{T}} + \mathbf{T}_{sgs}) \\ + \mathbf{f}_b \end{aligned} \quad (3)$$

where  $\tilde{\mathbf{v}}$ ,  $\tilde{p}$  is the filtered velocity and pressure, respectively.  $\mathbf{I}$  is the identity tensor,  $\tilde{\mathbf{T}}$  is the filtered stress tensor,  $\mathbf{f}_b$  is the resultant of the body forces.

The filtered equations are rearranged into a form that looks identical to the unsteady RANS equations. However, the turbulent stress tensor now represents the subgrid scale stresses. These stresses result from the interaction between the larger, resolved eddies and the smaller, unresolved eddies and are modeled using the Boussinesq approximation as follows:

$$\mathbf{T}_{sgs} = 2\mu_t \mathbf{S} - \frac{2}{3}(\mu_t \nabla \cdot \tilde{\mathbf{v}}) \mathbf{I} \quad (4)$$

where  $\mathbf{S}$  is the strain rate tensor, computed from the resolved velocity field  $\tilde{\mathbf{v}}$ .

The subgrid scale turbulent viscosity  $\mu_t$  must be described by a subgrid scale model that accounts for the effects of small eddies on the resolved flow. The wall-adapting local-eddy viscosity (WALE) subgrid scale model is a more modern subgrid scale model that uses a novel form of the velocity gradient tensor in its formulation. The WALE subgrid scale model provides the following mixing-length type formula for the subgrid scale viscosity:

$$\mu_t = \rho \Delta^2 S_w \quad (5)$$

where  $\Delta$  is the length scale or grid filter width,  $S_w$  is a deformation parameter.

### 2.2 Schnerr-Sauer Cavitation Model

The Schnerr-Sauer cavitation model is based on a reduced Rayleigh-Plesset (RP) equation and neglects the influence of bubble growth acceleration, viscous effects, and surface tension effects (Schnerr & Sauer 2001). The Schnerr-Sauer cavitation model calculates both the bubble growth and collapse rates, encompassing single-component and multi-component materials. The growth rate of cavitation bubbles is determined through the inertia-controlled growth model:

$$v_r^2 = \frac{2}{3} \left( \frac{p_{sat} - p}{\rho_l} \right) \quad (6)$$

where  $p_{sat}$  is the saturation pressure corresponding to the temperature at the bubble surface,  $p$  is the pressure of the surrounding liquid and  $\rho_l$  is the liquid density. Schnerr-Sauer model is a simplification of the more general

Rayleigh-Plesset equation which accounts for the inertia, viscous effects, and surface tension effects. All these numerical methods have been extensively verified and validated in the paper by Liu et al (2023).

### 3 OPEN WATER CHARACTERISTICS

This section simulates the flow field of a typical benchmark propeller under both fully wet conditions and cavitation, and compares the results with experimental data to validate the reliability of the numerical methods.

#### 3.1 Geometry and Computational Domain

In the numerical prediction study of propeller TVC, the E779A propeller is one of the most frequently used propellers. It is characterized by its simple structure, easy modeling, and the availability of a substantial amount of experimental and simulation data for comparison. The E779A propeller is a four-bladed propeller with a diameter of 0.227 meters. The geometry of the propeller is illustrated in Figure 1, and the detailed main parameters are provided in Salvatore et al (2009).

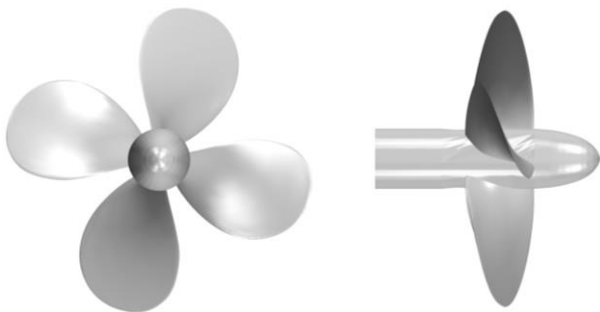


Figure 1 The INSEAN E779A propeller

To avoid the influence of reflected waves during the computation, the computational domain should be made as large as possible, simulating the propeller in an open-sea environment. The computational domain used in the numerical simulation consists of two parts. The first part is a cylindrical rotating domain (Rotation Region) with a length of 0.3 m and a radius of 0.15 m. Within this region, a rigid body motion approach is employed to simulate the rotational motion of the propeller. The second part is the surrounding farfield domain, which is a rectangular box with dimensions of 3 m × 1 m × 1 m.

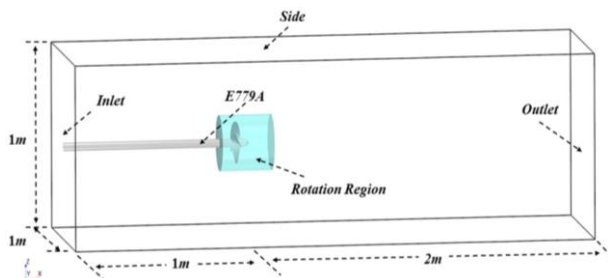


Figure 2 Computational domain

The two computational domains are connected through an interface to facilitate the transfer of flow field information. To minimize errors during computation, the inlets and outlets of the computational domain should be positioned as far away from the center of the propeller as possible. Therefore, the central point of the propeller is located 1 m

and 2 m away from the inlets and outlets of the computational domain, respectively, along the  $y$  and  $z$  directions as illustrated in Figure 2.

#### 3.2 Boundary and Initial Conditions

As shown in Figure 2, the inlet is configured as a velocity inlet, and depending on the operating conditions, the inlet velocity is specified based on the advance coefficients  $J$ . The outlet is set as a pressure outlet. Under open-water conditions, the outlet pressure is set to 0 Pa. However, during cavitation calculations, the outlet pressure is determined based on the cavitation number  $\sigma$ . The side boundary of the computational domain is treated as a slip wall, while the propeller surface is modeled as a non-slip and impermeable wall. The fluid is assumed to be fully turbulent and incompressible, with the cavitation simulation utilizing the volume of fluid (VOF) model. Cavitation conditions use an implicit unsteady approach with a second-order temporal discretization, a time step of  $\Delta t = 1 \times 10^{-4}$  s, 20 inner iterations per time step, and a total simulation duration of 0.2 s. Thrust and torque coefficients, as well as residuals are monitored throughout the simulation to assess convergence.

#### 3.3 Mesh Convergence Study

In this study, the discretization of the computational domain is conducted based on the unstructured trimmer mesh and custom volumetric refinement techniques within the Simcenter STAR-CCM+. The base size for the mesh is set to 0.016 m, with a maximum grid size of 0.064 m. To better capture the local flows near the propeller blades, the mesh around the propeller blades is refined. Specifically, the mesh size on the propeller blade surfaces and the feature curves of the blades is set to 0.001 m.

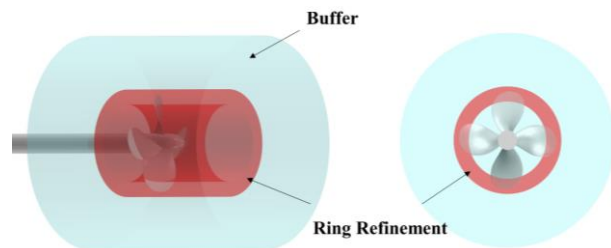


Figure 3 Custom refinement shapes

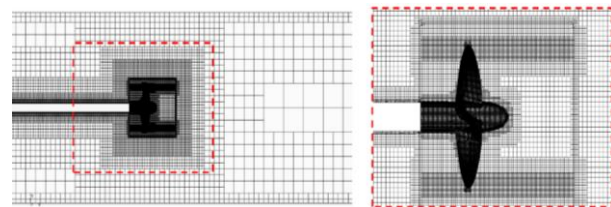


Figure 4 Mesh after first time refinement

Moreover, a buffer layer (Buffer Region) and a ring refinement (Ring Refinement Region) are added around the propeller and tip domain, as illustrated in Figure 3. The buffer layer is represented by a blue cylindrical structure with a length of 0.5 m and a radius of 0.25 m. The mesh size within the Buffer Region is set to 0.008 m, aiming to refine the solution for pressure and velocity variations during the rotation of the propeller. The Ring Refinement

Region is a red annular structure with a length of 0.3 m, an inner diameter of 0.09 m, and an outer diameter of 0.125 m. It fully encompasses the portion where the tip vortices may occur. The mesh size within this region is set to 0.002 m, allowing for finer capture of the propeller tip vortex. Following these two steps of refinement, the initial mesh configuration is complete, resulting in a mesh with 3.76 M cells, as shown in Figure 4.

To validate the chosen turbulence model and the aforementioned mesh configuration, open water characteristics (OWC) of the propeller under fully wet conditions is firstly simulated. This process is used to ascertain the values of the thrust coefficient  $K_T$ , the torque coefficient  $K_Q$ , and the efficiency  $\eta$  under different advance coefficients. The relevant formulas are expressed as follows:

$$\begin{aligned} K_T &= \frac{T}{\rho \cdot n^2 \cdot D^4} \\ K_Q &= \frac{Q}{\rho \cdot n^2 \cdot D^5} \\ \eta &= \frac{J}{2\pi} \cdot \frac{K_T}{K_Q} \\ J &= \frac{V_A}{n \cdot D} \end{aligned} \quad (7)$$

wherein  $T$  and  $Q$  represents the thrust and torque on the propeller, respectively,  $n$  is the rotation speed,  $D$  is the propeller diameter, and  $J$  is the advance coefficients.

Table 1 gives the open water performance for the two most commonly used advance coefficients, along with a comparison with experimental results by Salvatore et al (2009). The results correspond well with experimental values. For a more intuitive error analysis, consider the thrust coefficient at advance coefficients of 0.71, where the disparity between LES and experimental data amounts to 4.6%.

**Table 1 Computational results at two advance coefficients**

$J$	Exp	LES	
		$K_T$	Error
0.6	0.293	0.309	5.5%
0.71	0.238	0.249	4.6%

Set the inlet velocity to  $V_{inlet} = 5.8$  m/s ( $J = 0.71$ ), outlet pressure  $P_{outlet} = 62038$  Pa ( $\sigma = 1.763$ ). Use the  $Q$  criterion ( $Q = 50000$  m/s<sup>2</sup>) and volume fraction of vapor phase  $\alpha_v = 0.1$  to extract the tip vortex and cavity topology of the propeller, as shown in Figure 5. As shown in Figure 5(a), both the tip vortex and hub vortex of the propeller can be precisely captured. The tip vortex extends smoothly in a helical tube shape for a considerable downward distance, while the hub vortex appears as a cylindrical shape. The tip vortex gradually disappears after reaching the end of the ring refinement region, indicating that the mesh size in the region can effectively capture the tip vortex. In contrast, as shown in Figure 5(b), the propeller also exhibits obvious cavitation, but the cavities are mainly concentrated nearby the propeller blade surface. In the rotation process, the propeller undergoes a noticeable sheet cavitation, but the

TVC is not captured due to lack of resolution. According to the experimental results, there is a significant difference between the predicted and experimental results. This demonstrates that although the mesh size in the annular refinement region can effectively capture the tip vortex, it cannot capture the TVC. Therefore, it is necessary to further refine the mesh at the tip vortex region of the propeller. To minimize cell numbers, the optimal shape for mesh refinement should ideally match the shape of the tip vortex. However, since the tip vortex in the simulation can only be extracted using an isosurface method, it is difficult to produce a matched geometric shape that perfectly conforms to the tip vortex, so another regular geometric body should be used for the mesh refinement. Currently, the helical tube refinement method is one of the commonly used refinement methods in TVC simulation.

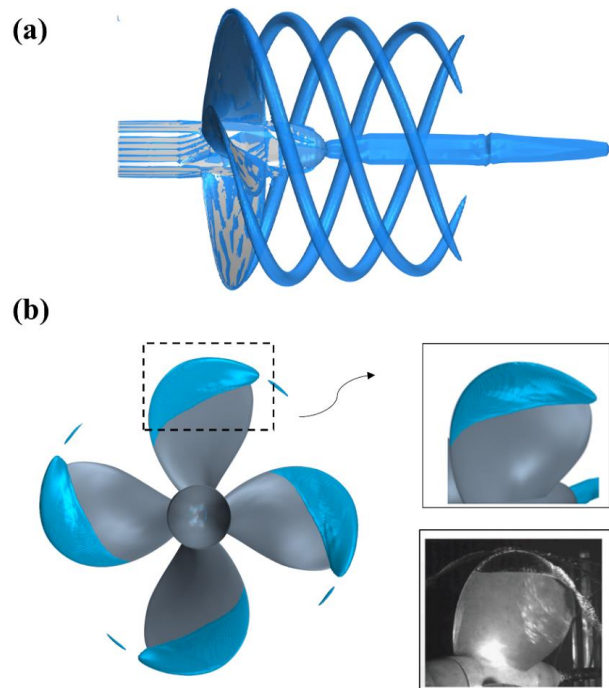


**Figure 5 Tip vortex and TVC of INSEAN E779A propeller: (a)  $Q = 50000$  m/s<sup>2</sup>; (b)  $\alpha_v = 0.1$**

Most researches use a constant diameter helical tube in the refinement process. However, as indicated in Figure 5, the tip vortex of the propeller does not exhibit a simple constant diameter helical tube shape as it develops downstream. Instead, as the tip vortex continues to evolve, its rotational diameter shows a trend of continuous reduction. Using a constant diameter helical tube for tip vortex refinement requires defining a larger tube diameter, leading to increased mesh cells. Therefore, this paper modifies the formula for the helical tube, establishing a relationship between the helical line's rotational radius and the forward distance as follows:

$$\begin{aligned} x &= a\theta \\ y &= r\cos(\theta) \\ z &= r\sin(\theta) \end{aligned} \quad (8)$$

where  $\theta$  is the rotation angle of the helical line,  $r$  is the rotational radius of the helical line, and  $a$  is the forward rate of the helical line. For a constant diameter helical line,

$r$  is a fixed value. However, in this case, since the helical line gradually contracts inward with the increase of  $x$ , it is necessary to establish the relationship between the rotational radius  $r$  of the helical line and the forward distance  $x$ . This paper simplifies the relationship between them into a linear relationship as follows:

$$r = c - kx \quad (9)$$

where  $c$  is the initial radius of the helical line, and  $k$  is the contraction rate. According to the formula, the second time refined helical tube of the propeller tip vortex is shown in Figure 6. In this case, the initial radius of the helical line is 0.111 m, the contraction rate is 0.009, and the rotation angle of the propeller is 180 degrees. Thus, the formed helical tube (in the green area) completely encloses the propeller tip vortex. The mesh size inside the helical tube is set to 0.5 mm, and the final mesh is shown in Figure 7, with a total cell count of 6.6 M. After that, validation needs to be performed again. The calculation results obtained from LES along with the experimental results (Yilmaz et al 2019) are shown in Table 2 and Figure 8.

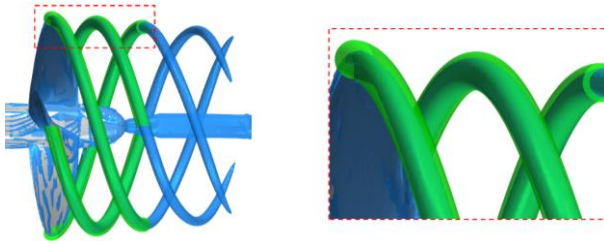


Figure 6 Shape of second time refinement

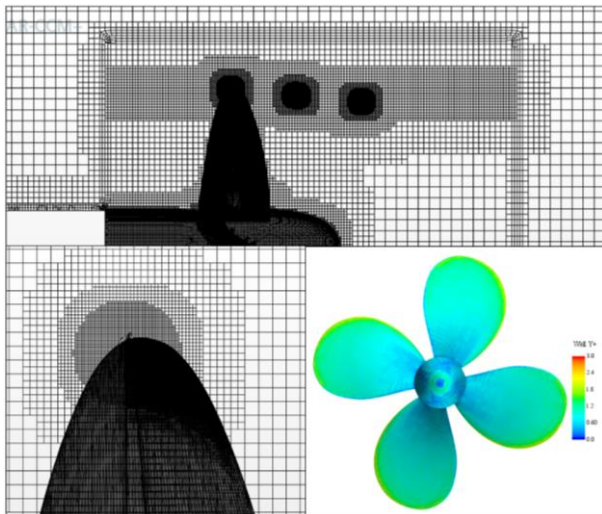


Figure 7 Final mesh in cavitation simulation

Table 2 Computational results comparison with experimental data ( $J = 0.71$ )

Item	Exp	CFD	Error
$K_T$	0.232	0.238	2.6%
$K_Q$	0.045	0.047	4.4%
$\eta$	58.3%	57.3%	1.7%

#### 4 TVC CONTROL BY ACTIVE WATER JETS

In the face of the prominent issue of TVC, seeking methods to control it to reduce the economic losses associated with propellers has become an important topic. This section focuses on the control of TVC by active water jets.

#### 4.1 Location of Injection Holes

Three different kinds of locations of water injection holes, namely, at the tip of the blade (Top Injection), on the suction side near the tip (Suction Side Injection), and on the pressure side near the tip (Pressure Side Injection) are created, as illustrated in Figure 9. As depicted in the figure, all three configurations have 7 holes with a diameter of 0.5 mm each. The placement of the openings is determined based on the structure of the tip vortex cavities. According to the prediction results of TVC in Section 3, the openings for all three conditions are placed nearby the inception point of the cavities, with a 1 mm spacing between the holes.

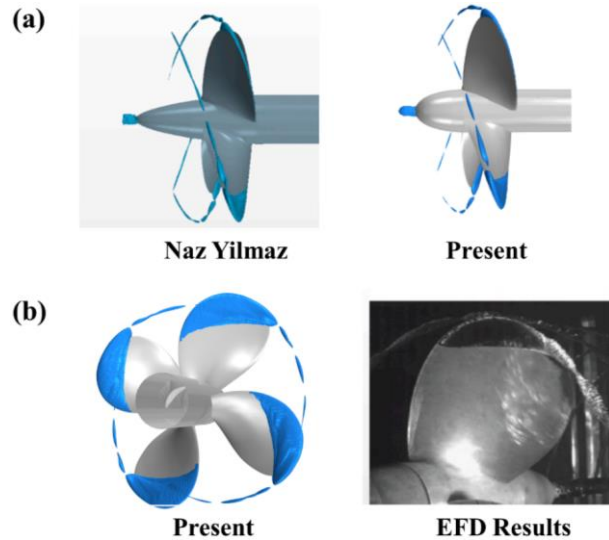
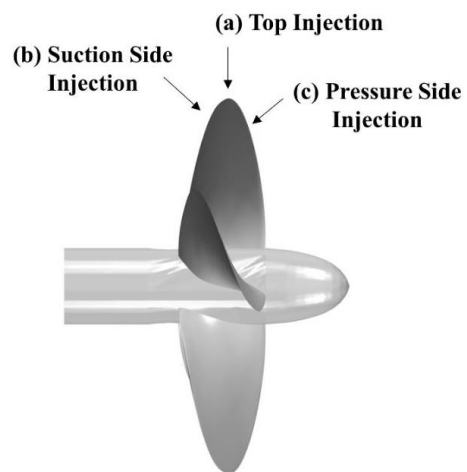


Figure 8 TVC comparison between present with other results: (a) Yilmaz et al (2019); (b) EFD results

The water jets velocity is specified based on the linear velocity at the blade tip position, given by  $V_t = \pi n D$ , and the maximum jet velocity  $V_j = 1.5 V_t$ . To mitigate computational divergence resulting from abrupt changes in jet velocity, it is defined that the jet velocity increases to the maximum linearly during the simulation. That is, at the beginning of the simulation, the jet velocity is zero, and after 0.18 s, it gradually increases to its maximum value.



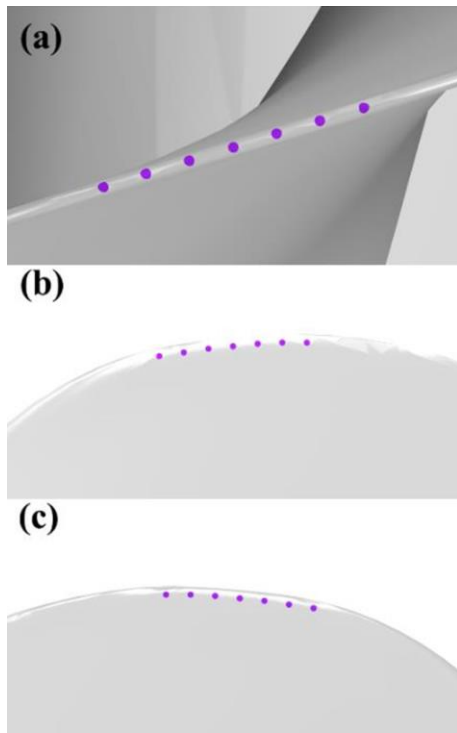


Figure 9 Locations of injection holes, (a) Top Injection; (b) Suction Side Injection; (c) Pressure Side Injection

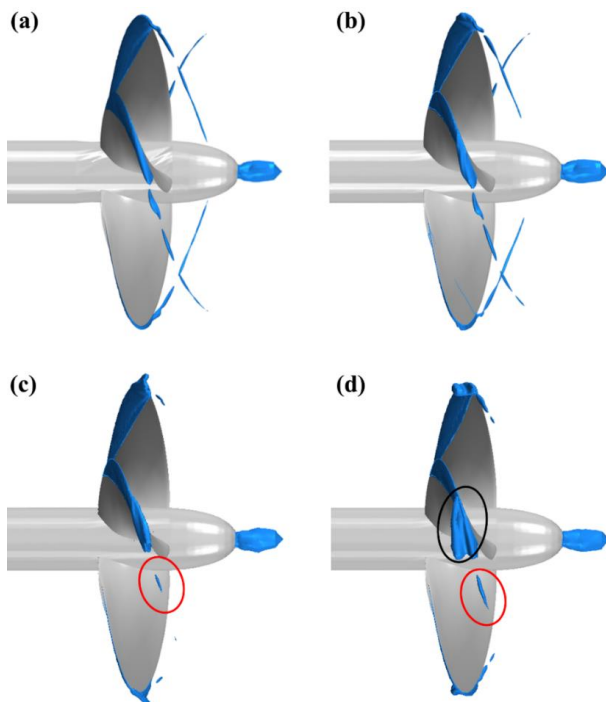


Figure 10 TVC structures comparison, (a) Without Injection; (b) Top Injection; (c) Pressure Side Injection; (d) Suction Side Injection

#### 4.2 TVC Comparison

To investigate the control effects of three active water jet configurations on TVC, isosurfaces based on volume fraction of vapor phase ( $\alpha_v = 0.1$ ) are extracted. Figure 10 illustrates the structures of TVC under four conditions: Without Injection, Top Injection, Pressure Side Injection and Suction Side Injection. As shown in the figure, there is an obvious control effect of active water jets on TVC. Both

top jet and lateral jet demonstrate varying degrees of suppression on the TVC, effectively reducing the length of the cavities. Firstly, by comparing Figure 10(a) and (b), it is evident that, in the case of top jet flow, the structure of tip vortex cavities undergoes minimal changes compared to the condition without jet. The morphology and development length of the tip vortex remain very similar. It indicates that top jet does not effectively control the development of TVC. On the other hand, in the cases of pressure side jet and suction side jet, as shown in Figure 10(c) and (d), the development length of tip vortex cavities is significantly reduced, as highlighted by the red boxes in the figure.

#### 4.3 OWC Performance

As a crucial propulsion component for ships, the influence of active water jets on the hydrodynamic performance is equally noteworthy. To determine the impact of top, suction side, and pressure side jets on the hydrodynamic performance, the thrust and torque coefficients on the propeller under these three conditions are provided in

Figure 11 and Figure 12. Under the four conditions, the thrust and torque coefficients show a gradually decreasing trend with time before 0.05 s, and gradually reaches to the stability state and shows a trend of oscillation. It can be seen from the results that the changing trends of thrust and torque coefficients under three conditions of no jet, pressure side jet and suction side jet are similar, that is, both pressure side jet and suction side jet have little influence on the hydrodynamic performance. While for the top jet condition, although its thrust and torque coefficients are reduced to a certain extent compared with other conditions, the reduction is limited. The findings demonstrate that active water jets exert a more pronounced influence on the local flow field near the opening position and its wake. However, they do not induce substantial alterations in the hydrodynamic performances.

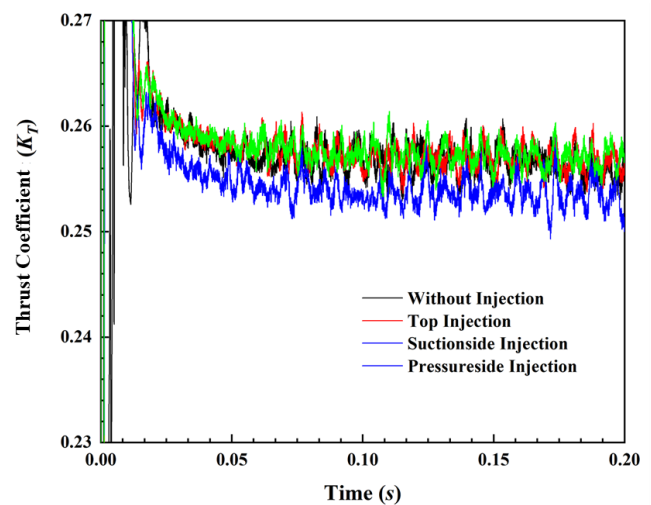


Figure 11 Thrust coefficient comparison under different injection condition

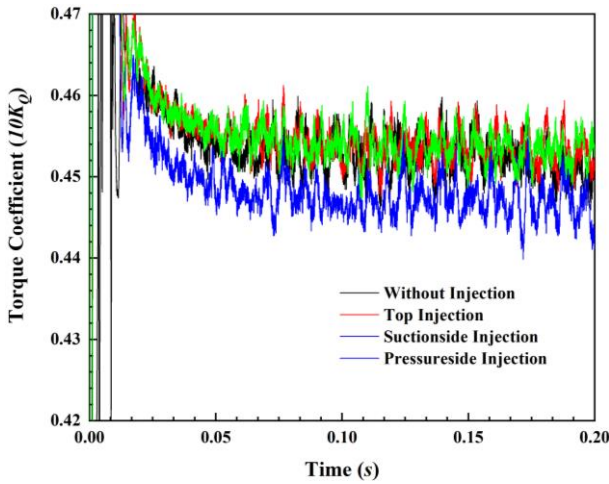


Figure 12 Torque coefficient comparison under different injection condition

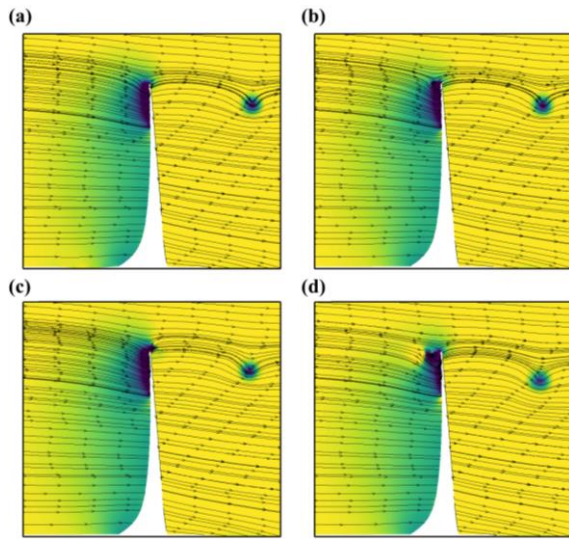


Figure 13 Flow field in tip region of E779A, (a) Without Injection; (b) Top Injection; (c) Pressure Side Injection; (d) Suction Side Injection

#### 4.4 TVC Evolution

To assess the impact of active jets on the flow field around the propeller, this section analyzes the local flow field near the propeller blades using streamline visualization. As shown in Figure 13, it presents pressure distribution contour and streamline variations near the surface of the propeller blades at  $y = 0$ .

Firstly, by comparing the changes in the pressure contour, it is apparent that the cross-sectional shape of the cavities (indicated by the purple area) under top jet condition is similar to the shape without jet. In the case of pressure side jet, due to the inductive effect of high-speed jet flow, the fluid tends to move towards the pressure side. As a result, there is a tendency for the low pressure region of the cavity under pressure side jet to extend beyond the tip of the propeller blade downstream. Since the jet velocity is opposite to the pressure side jet flow, the cross-sectional shape of the cavity under suction side jet condition tends to develop in the opposite direction to the incoming flow.

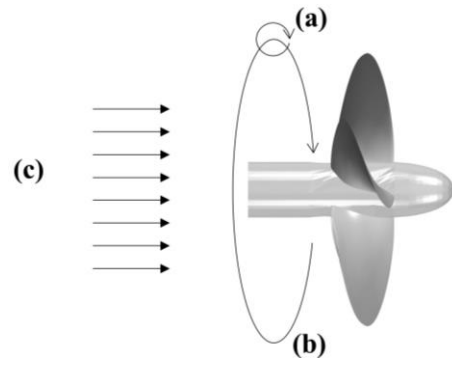


Figure 14 The flow trend of propeller tip vortex

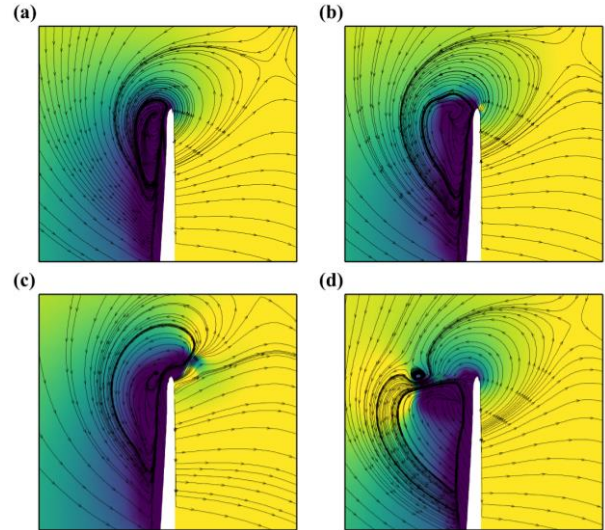


Figure 15 Flow field in tip region of E779A, (a) Without Injection; (b) Top Injection; (c) Pressure Side Injection; (d) Suction Side Injection

As shown in Figure 14, the propeller tip vortex is formed by the superposition of three types of movements: (a) the rotation generated by the tip vortex itself; (b) the rotational trend following the rotation of the propeller; and (c) the downstream flow following the incoming flow. Under the influence of these three movements, the propeller tip vortex develops in a helical line shape downstream. Additionally, because the axis of rotation of the tip vortex is perpendicular to the direction of the incoming flow, and the incoming flow velocity is greater than the rotational velocity, in the streamline visualization process, the inflow velocity obscures the lateral velocity fluctuations of the tip vortex, affecting the representation of its rotational movement. As shown in Figure 13, the streamlines in the figure only reflect the downstream movement trend of the tip vortex field and do not adequately capture its rotational effect. Therefore, to more clearly represent the high-speed rotational movement of the tip vortex, it is necessary to redefine the velocity vectors in the flow field by removing the inflow component from the velocity vectors, i.e.,  $Velocity_{[x]} = Velocity_{[x]} - V_I$ . The streamline plot with the redefined velocity vectors is shown in Figure 15.

As shown in Figure 15(a), the propeller tip vortex still exhibits a rotational movement trend from the pressure side to the suction side. In both pressure side jet and suction side jet conditions, the jet flow impedes the movement trend of

the tip vortex due to the different directions between the jet flow and the movement of the tip vortex at the local position of the jet orifice. Additionally, under the centrifugal force generated by the propeller's rotation, the TVC extends radially outward. Specifically, at the blade tip position, the fluid movement is roughly along the radial direction of the propeller due to the propeller rotation. In the case of top jet flow, where the jet flow direction coincides with the movement direction of the tip vortex, the impact of the jet on the tip vortex movement is minimal. This results in the fact that under top jet condition, the suppression effect on cavities is not as obvious as expected.

## 6 CONCLUSIONS

This paper focuses on the INSEAN E779A propeller, successfully conducting numerical calculations for the three-dimensional tip vortex and cavitation under both fully wetted and cavitation conditions. Through comparison with experimental data, the accuracy of the numerical methods and mesh configurations are validated. Given the limited research on the control of TVC using numerical methods, this paper simulates and analyzes TVC control under the influence of active water jets. The main conclusions are as follows.

Fully wetted and cavitation flow conditions of E779A propeller are investigated based on LES turbulent model and Schnerr-Sauer cavitation model, as well as a carefully designed mesh configuration. The results demonstrate that both the hydrodynamic and cavitation performance of the propeller are predicted very well and are in good agreement with literature and experimental results.

Three kinds of active water jets, namely top, pressure side, and suction side are selected to conduct numerical studies on the TVC control. The results indicate that, due to the overlap of the tip vortex with the top jets, the top jets have no effect on the development of TVC. In the cases of suction side and pressure side jets, not only the length of TVC is reduced, the jets also have an impact on the blade's sheet cavitation. Specifically, the suction side jets have a more significant effect on sheet cavitation.

## ACKNOWLEDGMENTS

This work is supported by National Natural Science Foundation of China (52131102), to which the authors are most grateful.

## REFERENCES

- Bensow, R.E. & Bark, G. (2010). 'Simulating cavitating flows with LES in OpenFOAM', V European Conference on Computational Fluid Dynamics, Lisbon, Portugal.
- Chahine, G. L., Frederick, G. F., & Bateman, R. D. (1993). 'Propeller tip vortex cavitation suppression using selective polymer injection', Journal of Fluids Engineering **115**.
- Franc, J. P. & Michel, J. M. (2006). Fundamentals of Cavitation, Springer science & Business media.
- Kadivar, E., El Moctar, O. & Javadi, K. (2018). 'Investigation of the effect of cavitation passive control on the dynamics of unsteady cloud cavitation', Applied Mathematical Modelling **64**.
- Lee, C. S., Ahn, B. K., Han, J. M., & Kim, J. H. (2018). 'Propeller tip vortex cavitation control and induced noise suppression by water injection', Journal of Marine Science and Technology **23**.
- Liu, K., Wei, P., Cao, L. & Wan, D. (2023). 'Tip vortex cavitation suppression and parametric study of an elliptical hydrofoil by water injection', Physics of Fluids **35**.
- Lu, S. P., Wang, W., & Wang, X. F. (2018). 'Experiment research on cavitation control by active injection', The 10th International Symposium on Cavitation, Maryland, USA.
- Park, S. L., Lee, S. J., You, G. S., & Suh, J. C. (2014). 'An experimental study on tip vortex cavitation suppression in a marine propeller', Journal of Ship Research **58**.
- Salvatore, F., Streckwall, H. & Van Terwisga, T. (2009). 'Propeller cavitation modelling by CFD-results from the VIRTUE 2008 Rome workshop', Proceedings of the First International Symposium on Marine Propulsors, Trondheim, Norway.
- Schnerr, G. H. & Sauer, J. (2001). 'Physical and numerical modeling of unsteady cavitation dynamics', Fourth International Conference on Multiphase Flow, New Orleans, USA.
- Timoshevskiy, M. V., & Zapryagaev, I. I. (2017). 'Generation of a wall jet to control unsteady cavitation over a 2D hydrofoil: Visualization and hydroacoustic signal analysis', Journal of Physics: Conference Series **899**. IOP Publishing.
- Wang, W., Tang, T., Zhang, Q. D., An, Z. Y., Tong, T. H., & Li, Z. J. (2020). 'Effect of water injection on the cavitation control: experiments on a NACA66 (MOD) hydrofoil', Acta Mechanica Sinica, **36**.
- Yilmaz, N., Atlar, M. & Khorasanchi, M. (2019). 'An improved mesh adaption and refinement approach to cavitation simulation (MARCS) of propellers', Ocean Engineering **171**.
- Zhang, X., Liu, Z., Cao, L. & Wan, D. (2022). 'Tip clearance effect on the tip leakage vortex evolution and wake instability of a ducted propeller', Journal of Marine Science and Engineering **10**.